ELSEVIER

Mixed conductivity and Mössbauer spectra of $(La_{0.5}Sr_{0.5})_{1-x}Fe_{1-y}Al_yO_{3-\delta}$ ($x = 0$–0.05, $y = 0$–0.30)

Vladislav V. Kharton[a,b,*], Joao C. Waerenborgh[c], Alexander P. Viskup[b],
Sergey O. Yakovlev[a], Mikhail V. Patrakeev[a,d], Piotr Gaczyński[c], Ivan P. Marozau[a],
Aleksey A. Yaremchenko[a], Aliaksandr L. Shaula[a], Victor V. Samakhval[b]

[a]Department of Ceramics and Glass Engineering, CICECO, University of Aveiro, 3810-193 Aveiro, Portugal
[b]Institute of Physicochemical Problems, Belarus State University, 14 Leningradskaya Street, 220050 Minsk, Belarus
[c]Chemistry Department, ITN/CFMC-UL, Estrada Nacional 10, P-2686-953 Sacavém, Portugal
[d]Institute of Solid State Chemistry, Ural Division of RAS, 91 Pervomaiskaya Street, Ekaterinburg 620219, Russia

Abstract

Aluminum incorporation in the rhombohedrally distorted perovskite lattice of $(La_{0.5}Sr_{0.5})_{1-x}Fe_{1-y}Al_yO_{3-\delta}$ ($x = 0-0.05$, $y = 0-0.30$) decreases the unit cell volume and partial ionic and p-type electronic conductivities, while the oxygen nonstoichiometry and thermal expansion at 900–1200 K increase on doping. The creation of A-site cation vacancies has an opposite effect on the transport properties of Al-substituted ceramics. The maximum A-site deficiency tolerated by the $(La,Sr)(Fe,Al)O_{3-\delta}$ structure is however limited, close to 3–4%. The Mössbauer spectroscopy revealed progressive localization of electron holes and a mixed charge-compensation mechanism, which results in higher average oxidation state of iron when Al^{3+} concentration increases. The average thermal expansion coefficients of $(La_{0.5}Sr_{0.5})_{1-x}Fe_{1-y}Al_yO_{3-\delta}$ are $(12.2–13.0) \times 10^{-6} K^{-1}$ at 300–900 K and $(20.1–30.0) \times 10^{-6} K^{-1}$ at 900–1200 K in air. The steady-state oxygen permeability (OP) of dense Al-containing membranes is determined mainly by the bulk ionic conductivity. The ion transference numbers at 973–1223 K in air, calculated from the oxygen permeation and faradaic efficiency (FE) data, vary in the range 1×10^{-4}–3×10^{-3}, increasing with temperature.
© 2006 Elsevier Inc. All rights reserved.

Keywords: Lanthanum–strontium ferrite; Perovskite; Mixed conductor; Oxygen ionic conductivity; Electronic transport; Mössbauer spectroscopy

1. Introduction

Partial oxidation of methane to synthesis gas (syngas), a mixture of CO and H_2, may take place efficiently on the surface of a mixed oxygen-ion/electron conducting membrane, which integrates oxidation with controlled oxygen separation in a single reactor [1–5]. The simplicity of the system implies significant savings in energy and capital compared to the conventional syngas production method of steam reforming of methane. Commercialization of such membrane devices, however, requires achieving the often

incompatible aims of high oxygen permeability, chemical stability and moderate thermal expansion for both oxidizing and reducing conditions, respectively encountered at the membrane feed and permeate sides. One group of promising materials with high oxygen permeability is the perovskite system based on lanthanum–strontium ferrite [6–11]. The ideal composition has not been fully established for the range of oxygen partial pressures relevant to membrane-reactor operation. A maximum of electronic and oxygen ionic conductivity in undoped $La_{1-x}Sr_xFeO_{3-\delta}$ was observed for $x = 0.5$ [10]; further strontium doping results in oxygen vacancy ordering and deterioration of transport properties [11]. In addition, high Sr contents are often associated with poorer thermodynamic and dimensional stability under the large oxygen chemical potential gradients required for reactor operation [12,13].

*Corresponding author. Department of Ceramics and Glass Engineering, CICECO, University of Aveiro, 3810-193 Aveiro, Portugal.
Fax: +351 234 425300.
E-mail address: kharton@cv.ua.pt (V.V. Kharton).

One established strategy to improve thermomechanical and, often, transport properties is the partial substitution of Fe with more redox-stable cations. These include other transition-metal cations, e.g. chromium and titanium [11,12,14] and isovalent species such as aluminium and gallium [8,9,13,15–18]. In the cases of Cr- [9,19] and Al-containing materials [18], the polarizing nature of the dopant tends to lower ionic conductivity. At the same time, incorporation of Al^{3+} into the perovskite-type $SrFe_{1-y}Al_yO_{3-\delta}$ enhances the phase stability at low oxygen chemical potentials and the ceramics sinterability [20]. The maximum solubility of aluminum cations in the perovskite lattices of $La_{1-x}Sr_xFe_{1-y}Al_yO_{3-\delta}$ ($x = 0.7$ -1.0) corresponds to $y = 0.30-0.35$ [18,20]. Although doping with gallium increases ionic conduction by promoting greater disorder in the oxygen sublattice of ferrites [8] and may thus be preferable from the oxygen permeability point of view, this element is rather expensive and volatile under highly reducing conditions and at high temperatures [21]. A similar enhancement of the ionic conductivity in $SrFeO_3$-based phases is also observed due to the creation of minor A-site cation deficiency, which suppresses to some extent the ordering processes in the oxygen sublattice [22]. For instance, in $Sr_{1-x}Fe_{1-y}Ti_yO_{3-\delta}$ system the highest ionic transport under oxidizing conditions is observed for compositions with $x \approx 0.03$ and $y = 0.20$ [22].

The present work was focused on the studies of transport properties and thermal expansion of cation-stoichiometric and A-site deficient $(La_{0.5}Sr_{0.5})_{1-x}Fe_{1-y}Al_yO_{3-\delta}$ perovskites. Particular attention was focused on the effects of Al doping and A-site cation vacancies on the iron oxidation states, oxygen nonstoichiometry, and oxygen ionic conductivity. In order to assess the charge compensation mechanisms and defect chemistry at low temperatures, the Mössbauer spectroscopy was used. In the high-temperature range, 973–1223 K, the defect formation mechanisms were evaluated using thermogravimetric analysis (TGA), coulometric titration (CT) and measurements of total conductivity and Seebeck coefficient as function of the oxygen partial pressure.

2. Experimental

Samples in the $(La_{0.5}Sr_{0.5})_{1-x}Fe_{1-y}Al_yO_{3-\delta}$ ($x = 0-$ 0.05, $y = 0-0.30$) system were synthesized by the glycine-nitrate process (GNP). Glycine was added as the fuel and chelating agent in 100% excess to an aqueous solution of the metal nitrate precursors in appropriate ratios. The solution was dried and heated until auto-ignition occurred, leaving a foam-like reaction product; this powder was annealed in air at 1273 K for 2 h to remove remaining organic content. Following several additional firing/regrinding steps, the resultant powders were ball-milled and pressed into disks (100–300 MPa); the gas-tight ceramics with density higher than 93% of theoretical were sintered in air at 1793–1823 K for 5 h. The samples were finally annealed in air at 1273 K for 3–4 h and slowly

cooled in order to achieve equilibrium with air at low temperatures.

Characterization of the materials was conducted employing X-ray diffraction (XRD) analysis (Rigaku Geiger-flex D/MAX-B), scanning electron microscopy coupled with energy dispersive spectroscopy (SEM/EDS, Hitachi S-4100), TGA (Setaram TG-92 and Setaram SetSys 16/18 instruments), and dilatometry (Linseis L70/2001, heating rate of 5 K/min). Investigation of the transport properties involved measurements of total conductivity (4-probe DC), Seebeck coefficient and steady-state oxygen permeation (OP) fluxes as functions of temperature and oxygen partial pressure. Detailed descriptions of experimental techniques and equipment can be found in previous publications [8–10,14,16–18,20,22,23]. The structural parameters were refined from XRD data using the Fullprof [23] and GSAS [24] software. For all the presented oxygen-permeability results, the membrane feed-side oxygen partial pressure (p_2) was maintained at 0.21 atm (atmospheric air). The ion transference numbers calculated from the oxygen permeation data were validated by the faradaic efficiency (FE) measurements under zero $p(O_2)$ gradient in air [20]. The total conductivity and thermopower were studied at 300–1300 K in an oxygen partial pressure ranging from 10^{-20} to 0.5 atm, as described elsewhere [17]. The criteria for equilibration of a sample after a change in either oxygen partial pressure or temperature included the relaxation rates of the conductivity and Seebeck coefficients less than 0.05%/min and 0.001 μV/(K min), correspondingly. Due to possible compositional instabilities at oxygen partial pressures from 10^{-6} down to 10^{-11}–10^{-9} atm, which result in hysteresis phenomena and, possibly, non-equilibrium values of the conductivity and Seebeck coefficient, in the present paper this $p(O_2)$ range is excluded from consideration. At higher and lower $p(O_2)$ values the transport properties were found completely reproducible, within the limits of standard experimental error. The oxygen nonstoichiometry at 923–1223 K in the oxygen partial pressure range 8×10^{-5} to 0.7 atm was studied by the CT technique [17]; the reference point for the CT data arrays was determined by TGA. The results obtained by TGA and calculated from the CT data showed an excellent agreement within all studied temperature range (Fig. 1), thus confirming zero leakage in the CT cells.

The Mössbauer spectra were collected at room temperature and at 10 K or, for samples with the lowest magnetic ordering temperatures, at 4.1 K. The measurements were performed in transmission mode using a conventional constant-acceleration spectrometer and 25 mCi ^{57}Co source in a Rh matrix. The velocity scale was calibrated using α-Fe foil. The absorbers were obtained by pressing the powdered samples (5 mg of natural Fe/cm^2) into perspex holders. Isomer shifts (IS, Table 1) are given relative to metallic α-Fe at room temperature. The low-temperature spectra were collected using either a liquid-helium flow cryostat with a temperature stability of ± 0.5 K to cool the samples down to 10 K or a JANIS bath cryostat, model SVT-400, with the
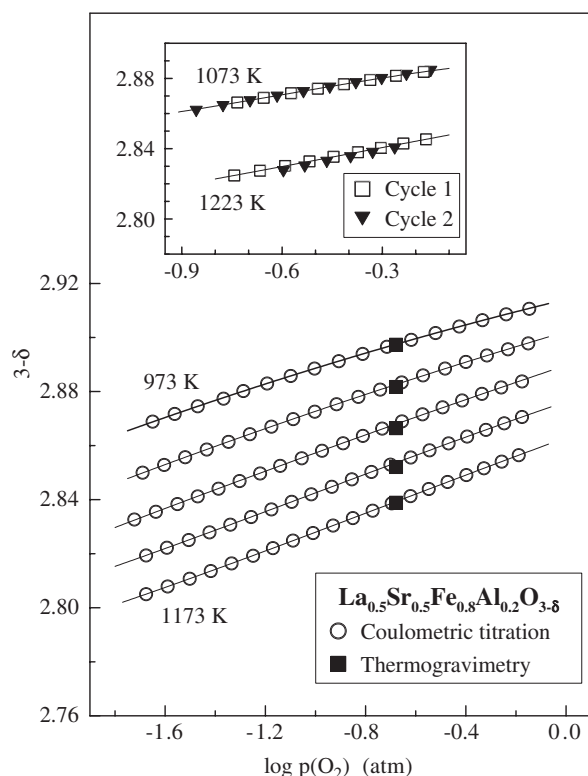
Fig. 1. Reproducibility of the total oxygen content values in $La_{0.5}Sr_{0.5}Fe_{0.8}Al_{0.2}O_{3-\delta}$, determined by TGA and calculated from the coulometric titration data using the reference point at 1223 K. The inset shows reproducibility of the oxygen content values measured by coulometric titration at starting (Cycle 1) and after finishing the measurements (Cycle 2).

sample immersed in liquid He for measurements at 4.1 K. The spectra were fitted to Lorentzian lines using a nonlinear least-squares method [25]. The relative areas and widths of both peaks in a quadrupole doublet were kept equal during refinement. Distributions of magnetic splittings were fitted according to the histogram method [26].

3. Results and discussion

3.1. Structure, thermal expansion and total conductivity

XRD analysis of the ceramic materials equilibrated with atmospheric oxygen at low temperatures, confirmed the formation of single perovskite phases, except for $(La_{0.5}Sr_{0.5})_{0.95}Fe_{0.7}Al_{0.3}O_{3-\delta}$ where minor impurity peaks attributed to monoclinic $SrAl_2O_4$ (PDF card 74-0794) are visible in the XRD patterns. Similar conclusion was drawn from the results of SEM/EDS analysis. As an example, Fig. 2 compares typical SEM micrographs of $(La_{0.5}Sr_{0.5})_{0.95}$ $Fe_{0.7}Al_{0.3}O_{3-\delta}$ and parent composition, $La_{0.5}Sr_{0.5}$ $FeO_{3-\delta}$; the small inclusions at the grain boundaries of major perovskite phase in $(La_{0.5}Sr_{0.5})_{0.95}Fe_{0.7}Al_{0.3}O_{3-\delta}$ ceramics (Fig. 2b) are aluminum-enriched. The maximum

A-site deficiency in heavily doped $(La,Sr)(Fe,Al)O_{3-\delta}$ perovskites is hence limited, close to 3–4%. This level is substantially lower than that in $Sr(Fe,Ti)O_{3-\delta}$ system [22], but comparable to $Sr(Fe,Al)O_{3-\delta}$ [20]. Neither grain-boundary anomalies nor essential compositional inhomogeneities were found for other studied compositions. The average grain size varied in the range 5–12 μm.

The perovskite-type structure of the title materials was identified as rhombohedrally distorted (space group $R\bar{3}c$). The incorporation of Al^{3+} having a smaller radius compared to iron cations [27] leads to the unit cell contraction, Table 2. An opposite effect is observed on the creation of A-site cation vacancies due to increasing anion repulsion forces.

Table 2 summarizes the average thermal expansion coefficients (TECs) of $(La_{0.5}Sr_{0.5})_{1-x}Fe_{1-y}Al_yO_{3-\delta}$ ceramics, calculated from the dilatometric data (Fig. 3). The increase in TEC at temperatures above 700–900 K is common among ferrite perovskites (e.g. [9,16]), and results from chemically induced expansion of the lattice due to oxygen loss and concomitant reduction of the iron sublattice. Surprisingly, this effect tends to increase on Al doping, suggesting that oxygen losses on heating increase with aluminum content. The latter phenomenon indicates that the average oxidation state of iron cations at low temperatures increases with aluminum additions, in agreement with the Mössbauer spectroscopy results discussed below.

The temperature dependencies of the total conductivity of the title series at atmospheric oxygen pressure are presented in Fig. 4. The oxygen transference numbers (t_o), calculated from the oxygen permeability and FE data, show that the ionic contribution is lower than 0.5% at 1223 K and decreases with decreasing temperature. Hence, the total conductivity is predominantly electronic, exhibiting semiconductor-type behavior in the low-temperature range until an apparent transition to metallic-like conduction is observed above 700–800 K. This trend originates, again, from oxygen loss on heating, which reduces the concentration of p-type electronic charge carriers [9,11,17]. Note that the transition temperature coincides around that of the change in the thermal-expansion regime. The activation energies in the low-temperature range, calculated by the standard Arrhenius equation, are listed in Table 3.

In agreement with literature data [28,29], the substitution of iron with Al^{3+} cations decreases the conductivity as the concentration of B sites participating in the electronic transport processes becomes lower (Fig. 4). In the case of $(La_{0.5}Sr_{0.5})_{0.97}FeO_{3-\delta}$, creation of A-site vacancies also leads to a lower p-type electronic conduction, indicating that the charge compensation occurs primarily via the formation of oxygen vacancies. On the contrary, the conductivity of $(La_{0.5}Sr_{0.5})_{1-x}Fe_{0.7}Al_{0.3}O_{3-\delta}$ ceramics is higher than that of the A-site stoichiometric analogue; this suggests that Al doping increases the role of alternative charge-compensation mechanism, via the hole generation.

Table 1
Parameters obtained from the Mössbauer spectra of $(La_{0.5}Sr_{0.5})_{1-x}Fe_{1-y}Al_yO_{3-\delta}$ perovskites

Composition	T (K)	Iron oxidation state	IS, <IS> (mm/s)	QS, ε (mm/s)	$<B_{hf}>$ (T)	Γ (mm/s)	I (%)	$3-\delta$
$La_{0.5}Sr_{0.5}FeO_{3-\delta}$	10	3+	0.42	−0.03	50.7		75	3.00
		5+	−0.02	−0.03	28.2		25	
	297	3+	0.29	0.12	—	0.36	50	
		4+itinerant	0.10	0.09	—	0.36	50	
$La_{0.5}Sr_{0.5}Fe_{0.8}Al_{0.2}O_{3-\delta}$	4.1	3+	0.42	−0.03	48.7		62	2.97
		4+localized	0.09	−0.09	31.4		20	
		5+	−0.02	0.02	26.9		18	
	297	3+	0.31	0.40	—	0.48	43	
		4+localized	−0.03	0.22	—	0.38	20	
		4+itinerant	0.14	0.32	—	0.46	37	
$La_{0.5}Sr_{0.5}Fe_{0.7}Al_{0.3}O_{3-\delta}$	4.1	3+	0.41	0.02	47.8		59	2.96
		4+localized	0.10	0.00	31.6		21	
		5+	−0.04	0.03	27.5		20	
	297	3+	0.30	0.51	—	0.46	39	
		4+localized	−0.04	0.28	—	0.37	21	
		4+itinerant	0.13	0.35	—	0.47	40	
$(La_{0.5}Sr_{0.5})_{0.97}Fe_{0.7}Al_{0.3}O_{3-\delta}$	4.1	3+	0.41	0.00	48.1		58	2.95
		4+localized	0.13	−0.15	33.3		15	
		5+	−0.01	0.03	28.2		27	
	297	3+	0.29	0.38	—	0.42	32	
		4+localized	−0.03	0.21	—	0.35	15	
		4+itinerant	0.11	0.29	—	0.45	53	

Notes: IS, Γ and QS are the isomer shift relative to metallic α-Fe at 295 K, line-widths and the quadrupole splitting of a doublet in the paramagnetic state, respectively.
For the magnetically split spectra fitted with a distribution of sextets, the average isomer shift <IS>, the quadrupole shift ε and the average magnetic hyperfine field $<B_{hf}>$ are given.
I is the relative area.
Estimated errors are $\leqslant 0.2$ T for $<B_{hf}>$, <2% for I, and $\leqslant 0.02$ mm/s for the other parameters.
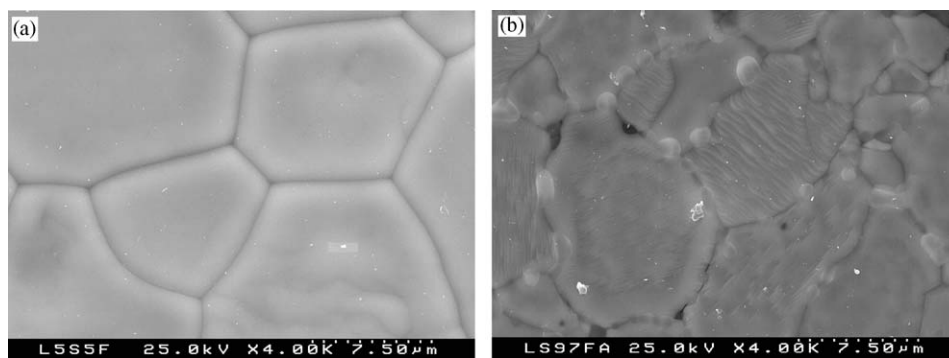
Fig. 2. SEM micrographs of $La_{0.5}Sr_{0.5}FeO_{3-\delta}$ (a) and $(La_{0.5}Sr_{0.5})_{0.95}Fe_{0.7}Al_{0.3}O_{3-\delta}$ (b) ceramics, polished and thermally etched at 1473 K.

3.2. Mössbauer spectra and oxygen nonstoichiometry

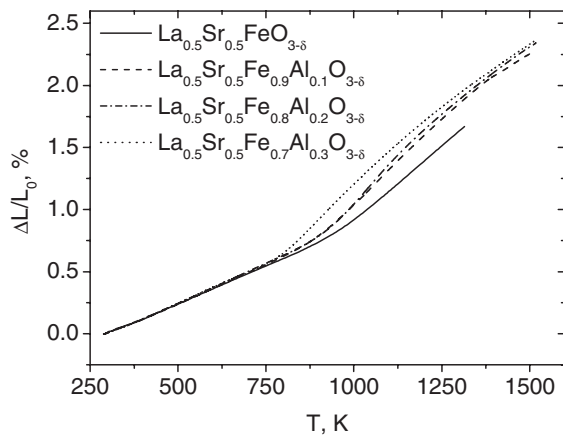The Mössbauer spectra of $La_{0.5}Sr_{0.5}FeO_{3-\delta}$ (Figs. 5 and 6) are similar to those reported by Dann et al. [30]. At 297 K, the spectrum consists of an Fe^{3+} doublet and another quadrupole doublet where the IS value is typical for Fe^{4+} with an electronic ground state having predominant itinerant $|d\ ^5L_>^{-1}$ character, as in $SrFeO_3$ [31,32]. At 10 K this perovskite is magnetically ordered (Fig. 6). The peaks of the sextets are broad, their widths strongly

increasing from the innermost to the outermost peaks. This effect is certainly due to disorder arising from the different near-neighbour configurations of iron cations, particularly from the presence of both Fe^{3+} and Fe^{4+} on the same crystallographic positions. For the spectrum at 10 K, the fitting quality using a distribution of magnetic hyperfine fields is substantially better than that by considering a single sextet whose peaks have very different widths. The average hyperfine parameters (Table 1) show that in addition to magnetic ordering, decreasing temperature

Table 2
Unit cell parameters and thermal expansion coefficients of $(La_{0.5}Sr_{0.5})_{1-x}Fe_{1-y}Al_yO_{3-\delta}$

Composition	Unit cell parameters		Average TECs in air	
	a (Å)	α (deg)	T (K)	$\bar{\alpha} \times 10^6 (K^{-1})$
$La_{0.5}Sr_{0.5}FeO_{3-\delta}$	5.4938	60.27	350–950	12.4
			950–1310	23.7
$(La_{0.5}Sr_{0.5})_{0.97}FeO_{3-\delta}$	5.4971	60.12	—	—
			—	—
$La_{0.5}Sr_{0.5}Fe_{0.9}Al_{0.1}O_{3-\delta}$	5.4810	60.20	350–900	13.0
			900–1200	27.6
			1200–1500	22.0
$La_{0.5}Sr_{0.5}Fe_{0.8}Al_{0.2}O_{3-\delta}$	5.4698	60.05	350–900	12.9
			900–1200	30.0
			1200–1500	22.3
$La_{0.5}Sr_{0.5}Fe_{0.7}Al_{0.3}O_{3-\delta}$	5.4540	60.07	350–800	12.7
			800–1200	27.1
			1200–1500	20.5
$(La_{0.5}Sr_{0.5})_{0.97}Fe_{0.7}Al_{0.3}O_{3-\delta}$	5.4651	60.13	350–800	12.2
			800–1350	24.8
$(La_{0.5}Sr_{0.5})_{0.95}Fe_{0.7}Al_{0.3}O_{3-\delta}$	5.4806	60.26	—	—
			—	—

Fig. 3. Dilatometric curves of $La_{0.5}Sr_{0.5}Fe_{1-y}Al_yO_{3-\delta}$ ceramics in air.

Fig. 4. Temperature dependencies of the total conductivity of $(La_{0.5}Sr_{0.5})_{1-x}Fe_{1-y}Al_yO_{3-\delta}$ ceramics in air.

leads to the charge disproportionation of Fe^{4+} cations, as previously reported for undoped $La_{0.5}Sr_{0.5}FeO_{3-\delta}$ [30]. At 10 K, a charge-ordered (CO) state is observed where 50% of the itinerant Fe^{4+} at 297 K, is detected as Fe^{3+} and the other 50% as Fe^{5+}. The latter contribution consists of a sextet with B_{hf} and IS lower than those typical for Fe^{4+} below 10 K [30–35]. The oxygen deficiency of $La_{0.5}Sr_{0.5}FeO_{3-\delta}$ equilibrated with air at low temperatures is negligible within the limits of experimental error.

As the Mössbauer spectra of Al-substituted materials below the magnetic ordering temperature are better resolved than those collected in the paramagnetic state, the analysis of doping effects should be started from the low-temperature data. When fitted with only two B_{hf}
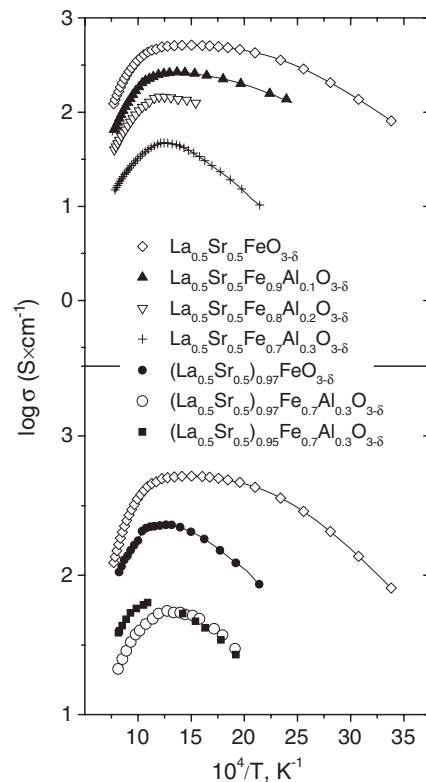
distributions as for the $La_{0.5}Sr_{0.5}FeO_{3-\delta}$ spectrum taken at 10 K, the distribution with lower B_{hf} is bimodal and shows a very strong dependence of IS on B_{hf}. A significantly

Table 3
Activation energy (E_a) of the total and oxygen ionic conductivities of $(La_{0.5}Sr_{0.5})_{1-x}Fe_{1-y}Al_yO_{3-\delta}$ in air

Composition	Total conductivity		Oxygen ionic conductivity	
	T (K)	E_a (kJ/mol)	T (K)	E_a (kJ/mol)
$La_{0.5}Sr_{0.5}FeO_{3-\delta}$	300–510	13.1	1073–1223	127
$(La_{0.5}Sr_{0.5})_{0.97}FeO_{3-\delta}$	470–620	16.5	1073–1223	93
$La_{0.5}Sr_{0.5}Fe_{0.9}Al_{0.1}O_{3-\delta}$	420–730	10.0	1023–1223	115
$La_{0.5}Sr_{0.5}Fe_{0.8}Al_{0.2}O_{3-\delta}$	—	—	1023–1223	119
$La_{0.5}Sr_{0.5}Fe_{0.7}Al_{0.3}O_{3-\delta}$	460–720	21.0	1023–1223	95
$(La_{0.5}Sr_{0.5})_{0.97}Fe_{0.7}Al_{0.3}O_{3-\delta}$	520–700	16.3	1073–1223	125
$(La_{0.5}Sr_{0.5})_{0.95}Fe_{0.7}Al_{0.3}O_{3-\delta}$	520–660	14.8	1173–1223	110
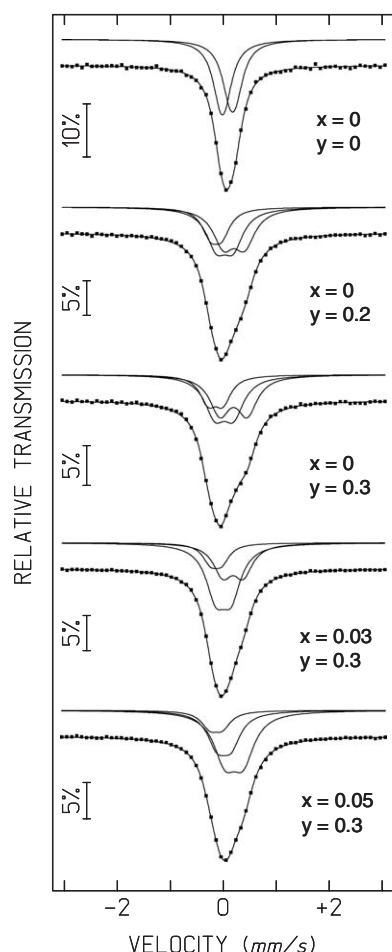
Fig. 5. Room-temperature Mössbauer spectra of $(La_{0.5}Sr_{0.5})_{1-x}Fe_{1-y}Al_yO_{3-\delta}$ perovskites. The calculated function plotted on the experimental points is the sum of two or three doublets corresponding to Fe^{3+}, and itinerant and localized Fe^{4+} (Table 1).

Fig. 6. Low-temperature Mössbauer spectra of $(La_{0.5}Sr_{0.5})_{1-x}Fe_{1-y}Al_yO_{3-\delta}$ (see text). The corresponding temperatures and calculated contributions are given in Table 1.

better agreement with experimental data was achieved when splitting this distribution into two, considering on the whole three magnetic hyperfine distributions. The estimated $<IS>$ and $<B_{hf}>$ of the third distribution are typical of localized Fe^{4+} at 4.1 K [31,33,34]. Due to the replacement of Fe by Al, the number of pathways for the (Fe 3d–O 2p) conduction electrons becomes smaller and, consequently, the electronic state of at least part of Fe^{4+}
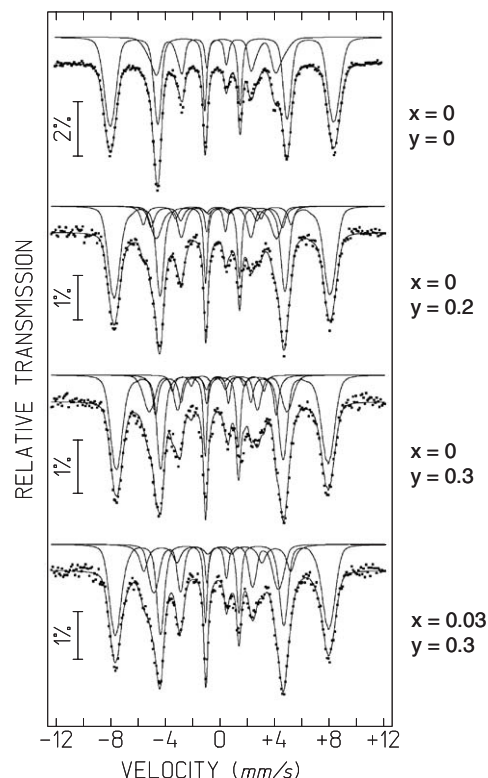
tends to a predominantly localized $|d_>^4$ character. In fact, the localization of the Fe^{4+} electronic state is only observed for about one third of the Fe^{4+} cations (Table 1), whereas approximately two thirds of the Fe^{4+} remain in an itinerant state disproportionating at low temperature. As for $Sr_{0.66}La_{0.33}Fe_{1-x}Co_xO_{3-\delta}$ [33], a microscopic phase separation seems to occur; the presence of Fe^{5+} contributions indicates that domains with higher Fe^{4+} concentration remain in the CO state.

According to these results, three different contributions should also appear in the paramagnetic state (Fig. 5), which was not possible to guess a priori due to the strong overlapping of the quadrupole doublets. Two different sets of these contributions are possible. The most probable combination comprises Fe^{3+}, localized Fe^{4+} and itinerant

Fe^{4+}. Less likely, if charge disproportionation is still preserved at room temperature, the contributions of Fe^{3+}, localized Fe^{4+} and Fe^{5+} should be present instead. Two series of simulations were, hence, performed constraining the relative areas and isomer shifts within narrow ranges consistent with the low-temperature data. The first combination, with itinerant Fe^{4+} at room temperature, provides the best-fit quality. The estimated parameters for the room-temperature spectra show an increase in the QS and Γ values with increasing Al^{3+} concentration, Table 1. This may result from increasing disorder due to the presence of two types of cations in the B sublattice, increasing oxygen-vacancy concentration and content of pentacoordinated iron ions.

Indeed, the oxygen nonstoichiometry of $(La_{0.5}Sr_{0.5})_{1-x}Fe_{1-y}Al_yO_{3-\delta}$, calculated from relative areas of the contributions detected in the Mössbauer spectra at 4–10 K, increases with increasing aluminum content (Table 1). The same tendency is observed when temperature increases up to 923–1223 K; Fig. 7 presents the $p(O_2)-T-\delta$ diagrams obtained by the CT technique. The doping-induced increase of the oxygen deficiency is expected to contribute to the conductivity decrease (Fig. 4) due to lowering concentration of the Fe–O–Fe bonds responsible for the hole conduction in perovskite-type ferrites. Similar trends were found earlier for other ferrite-based systems, such as $SrFe(Al)O_{3-\delta}$ and $La_{0.3}Sr_{0.7}Fe(Ga)O_{3-\delta}$ [17,32]. In contrast to these analogues, however, the average oxidation state of iron in $(La_{0.5}Sr_{0.5})_{1-x}Fe_{1-y}Al_yO_{3-\delta}$ system increases with increasing y (Table 1). This factor seems

responsible for increasing oxygen losses on heating and, thus, for the apparent increase in TECs in the intermediate-temperature range (Fig. 3). Note that at 300–700 K, the TECs of all title materials have similar values (Table 2). Although higher Fe^{4+} fraction should also lead to increasing electron–hole transport, the conductivity vs. composition dependence in A-site stoichiometric $La_{0.5}Sr_{0.5}Fe_{1-y}Al_yO_{3-\delta}$ is primarily determined by decreasing concentrations of iron cations when y increases.

In the case of $(La_{0.5}Sr_{0.5})_{0.97}Fe_{0.7}Al_{0.3}O_{3-\delta}$, the average oxidation state of iron and the fraction of itinerant Fe^{4+} are both higher than in $La_{0.5}Sr_{0.5}Fe_{0.7}Al_{0.3}O_{3-\delta}$ (Table 1). As a result, total conductivity of the A-site deficient composition is higher than that of the A-site stoichiometric perovskite where the Fe:Al concentration ratio is the same (Fig. 4). At the same time, creation of A-site vacancies results in a slight increase of the oxygen nonstoichiometry, indicating a mixed charge-compensation mechanism which involves the formation of holes and oxygen vacancies.

The Mössbauer spectroscopy data on $(La_{0.5}Sr_{0.5})_{0.95}Fe_{0.7}Al_{0.3}O_{3-\delta}$ cannot be used for quantitative comparison as this material is not single-phase. Although neither XRD nor Mössbauer spectroscopy give any evidence of Fe-containing phase impurities, the segregation of $SrAl_2O_4$ should change the La:Sr concentration ratio, affecting defect formation mechanisms. Nonetheless, in the intermediate-temperature range the conductivity of $(La_{0.5}Sr_{0.5})_{0.95}Fe_{0.7}Al_{0.3}O_{3-\delta}$ is close to that of $(La_{0.5}Sr_{0.5})_{0.97}Fe_{0.7}Al_{0.3}O_{3-\delta}$ (Fig. 4). On heating above 900 K the conductivity of the former material becomes even higher, probably due to progressive dissolution of $SrAl_2O_4$ in the perovskite lattice.

Finally, when comparing the results on $(La_{0.5}Sr_{0.5})_{1-x}Fe_{1-y}Al_yO_{3-\delta}$ and the data on other Al-substituted ferrite systems such as $La_{0.3}Sr_{0.7}Fe_{1-y}Al_yO_{3-\delta}$ and $SrFe_{1-y}Al_yO_{3-\delta}$ [18,20,32], one can conclude that increasing the La:Sr cation ratio shifts the redox equilibria involving B-site cations towards iron oxidation. In particular, Al doping decreases the Fe^{4+} fraction in $Sr(Fe,Al)O_{3-\delta}$ at atmospheric oxygen pressure [32]; the behavior of the title materials is opposite. Analogously, the A-site deficiency charge compensation mechanism undergoes a transition from predominantly ionic for $Sr_{1-x}Fe_{1-y}Al_yO_{3-\delta}$ [20] to mixed for $(La_{0.5}Sr_{0.5})_{1-x}Fe_{1-y}Al_yO_{3-\delta}$.

3.3. Electrical properties vs. oxygen partial pressure

Selected data for the oxygen-pressure dependence of the total conductivity and Seebeck coefficient of $(La_{0.5}Sr_{0.5})_{1-x}Fe_{1-y}Al_yO_{3-\delta}$ are presented in Figs. 8–10. The positive sign of the thermopower and the decreasing conductivity with decreasing $p(O_2)$ in the range 0.5–10^{-5} atm confirm that p-type electronic transport predominates in oxidizing regimes. Further reduction of the oxygen partial pressure leads to a conductivity minimum, as exhibited by other ferrite-based phases [9–11,17,28], where oxygen ionic conduction dominates
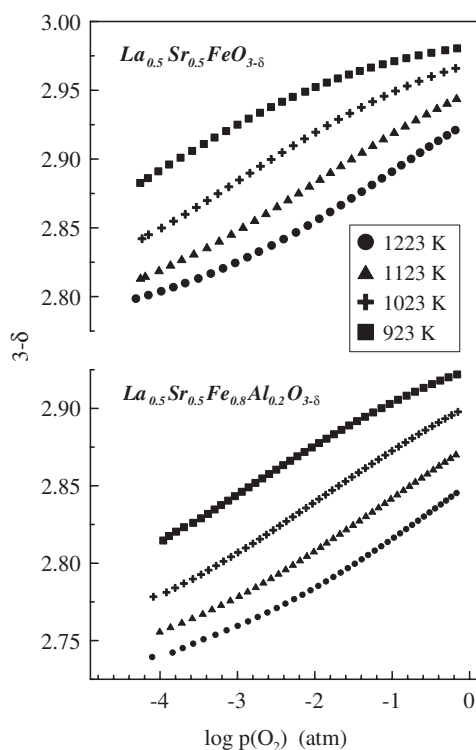

Fig. 7. The $p(O_2)-T-\delta$ diagrams of $La_{0.5}Sr_{0.5}FeO_{3-\delta}$ and $La_{0.5}Sr_{0.5}Fe_{0.8}Al_{0.2}O_{3-\delta}$ under oxidizing conditions.
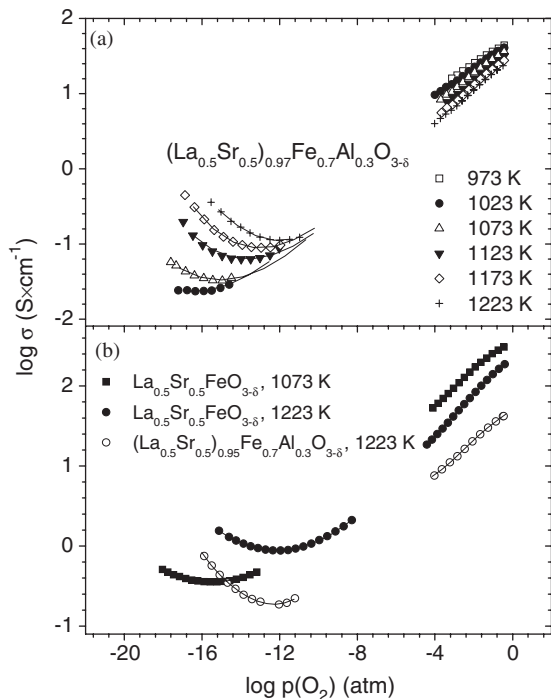
Fig. 8. Oxygen partial pressure dependencies of the total conductivity of $(La_{0.5}Sr_{0.5})_{0.97}Fe_{0.7}Al_{0.3}O_{3-\delta}$ (a), and comparison of the conductivity of $(La_{0.5}Sr_{0.5})_{0.95}Fe_{0.7}Al_{0.3}O_{3-\delta}$ and $La_{0.5}Sr_{0.5}FeO_{3-\delta}$ ceramics at 1073 and 1223 K (b). Solid lines are a guide for the eye.

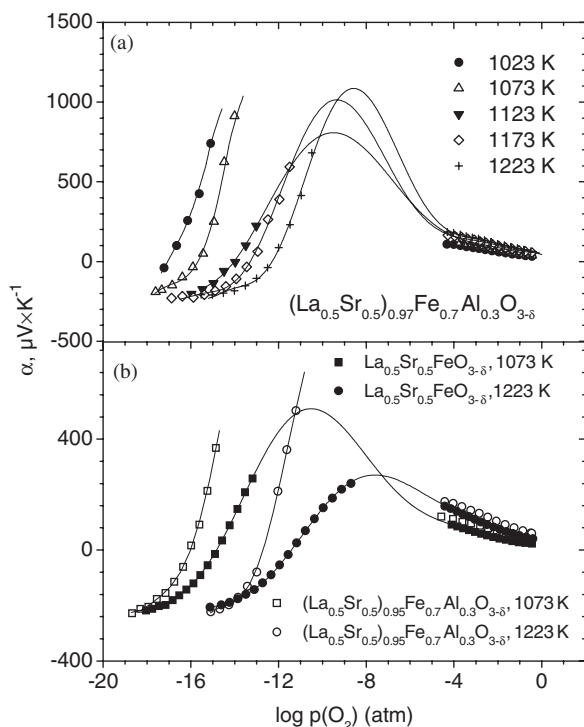Fig. 9. Oxygen partial pressure dependencies of the Seebeck coefficient of $(La_{0.5}Sr_{0.5})_{0.97}Fe_{0.7}Al_{0.3}O_{3-\delta}$ (a), and comparison of the thermopower of $(La_{0.5}Sr_{0.5})_{0.95}Fe_{0.7}Al_{0.3}O_{3-\delta}$ and $La_{0.5}Sr_{0.5}FeO_{3-\delta}$ (b). Solid lines are a guide for the eye.

and the contributions from p- and n-type electronic transport are comparable; beyond the minimum at still lower $p(O_2)$, conductivity increases due to the increasing participation of n-type charge carriers. These variations can be analyzed using the established defect model observed for other ferrite perovskites at elevated temperatures [9,11,36], describing the iron cation equilibria in terms of the oxidation and disproportionation reactions:

$$1/2O_2 + V_O + 2Fe^{3+} = O^{2-} + 2Fe^{4+},$$
$$2Fe^{3+} = Fe^{2+} + Fe^{4+}, \tag{1}$$
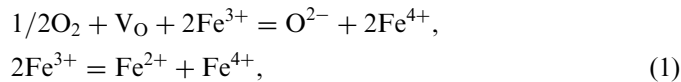
where Fe^{2+} and Fe^{4+} represent n- and p-type electronic charge carriers located on the iron cations. The corresponding equilibrium constants are expressed as

$$K_{ox} = \frac{[O^{2-}][Fe^{4+}]^2}{[V_O][Fe^{3+}]^2 p(O_2)^{1/2}}, \quad K_i = \frac{[Fe^{2+}][Fe^{4+}]}{[Fe^{3+}]^2}. \tag{2}$$

As for other partial conductivities, the p-type electronic conductivity (σ_p) is generally defined in terms of the hole concentration (p), charge and mobility (μ_p). Taking Eq. (2) into account, one can easily obtain

$$\sigma_p = ep\mu_p = e\mu_p \left(\frac{K_{ox}[V_O]}{[O^{2-}]} \right)^{1/2} [Fe^{3+}] p(O_2)^{1/4}, \tag{3}$$

where e is the elementary charge. In the range of oxygen partial pressures close to the minima in total conductivity, changes in the oxygen nonstoichiometry (δ) of ferrites and, consequently, $[V_O]$ and $[O^{2-}]$, are typically very small and the concentrations of Fe^{2+} and Fe^{4+} are considerably lower with respect to Fe^{3+} [9,11,34,36,37]. One may then simplify Eq. (3) to

$$\sigma_p = \sigma_p^0 p(O_2)^{1/4}, \tag{4}$$

where σ_p^0 is the hole conductivity at unit oxygen pressure. Analogously, the n-type electronic conductivity can be expressed with a similar equation as proportional to $p(O_2)^{-1/4}$. The ionic conductivity (σ_O) may be considered as independent of the oxygen chemical potential close to the minimum. The $p(O_2)$-dependence of the total conductivity can, thus, be approximated by the power model:

$$\sigma = \sigma_O + \sigma_p^0 p(O_2)^{1/4} + \sigma_n^0 p(O_2)^{-1/4}. \tag{5}$$

The conductivity of $(La_{0.5}Sr_{0.5})_{1-x}Fe_{1-y}Al_yO_{3-\delta}$ in reducing conditions was fitted with this model; several examples of fitting results at various temperatures are presented in Fig. 10. The experimental and calculated data are in excellent agreement. One should caution that, in general, the ionic conductivity in perovskite-type ferrites increases with reducing $p(O_2)$ due to increasing vacancy concentration. Also, for highly defective systems such as $(La_{0.5}Sr_{0.5})_{1-x}Fe_{1-y}Al_yO_{3-\delta}$, interaction between the defects may lead to the necessity to introduce activity coefficients in the mass action laws, Eq. (2). The data on ionic conductivity discussed below confirm a significant role of oxygen-vacancy clustering, typical for most heavily doped ferrite systems [6,9,11,13,18,22]. Eq. (5) should thus
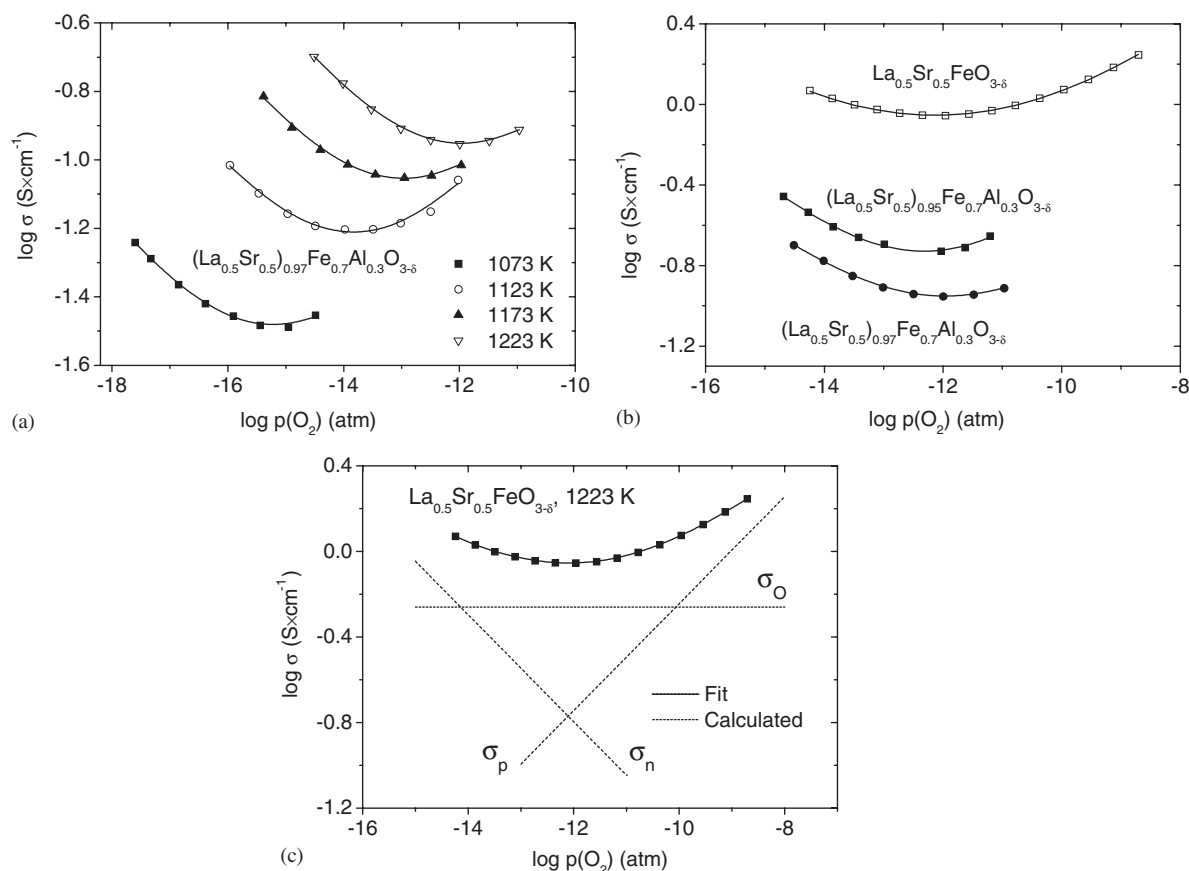
Fig. 10. Oxygen partial pressure dependencies of the total conductivity of $(La_{0.5}Sr_{0.5})_{0.97}Fe_{0.7}Al_{0.3}O_{3-\delta}$ in the vicinity of electron–hole equilibrium points (a), comparison of the total conductivity curves of $(La_{0.5}Sr_{0.5})_{1-x}Fe_{1-y}Al_yO_{3-\delta}$ ceramics at 1223 K (b), and experimental data points and calculated partial ionic, p-type and n-type electronic conductivities of $La_{0.5}Sr_{0.5}FeO_{3-\delta}$ at 1223 K (c). Solid lines correspond to fitting results using Eq. (5).

be considered as approximation only. However, as mentioned above, variations in the oxygen content in the $p(O_2)$ range close to the conductivity minimum are very small; hence, any changes in ionic conductivity and activity coefficients occurring with oxygen chemical potential in the fitted $p(O_2)$ range are expected to be negligible. Whatever the effects of ordering in the oxygen sublattice, the results unambiguously show that Al doping and creation of A-site vacancies in $La_{0.5}Sr_{0.5}FeO_{3-\delta}$ does not alter the electronic conduction mechanisms, except for the variations in the charge carrier concentration and mobility.

4. Oxygen ionic transport

Fig. 11 compares the steady-state OP fluxes, j, and specific oxygen permeabilities, $J(O_2)$, of dense $La_{0.5}Sr_{0.5}$ $FeO_{3-\delta}$ and $La_{0.5}Sr_{0.5}Fe_{0.9}Al_{0.1}O_{3-\delta}$ ceramics with various thicknesses; temperature dependence of the permeation fluxes through 1.0 mm thick $(La_{0.5}Sr_{0.5})_{1-x}Fe_{1-y}Al_yO_{3-\delta}$ membranes under a fixed $p(O_2)$ gradient is presented in Fig. 12. The oxygen permeability is related to oxygen flux density using the definition suggested by Möbius [38]

$$J(O_2) = jd\left[\ln\frac{p_2}{p_1}\right]^{-1}, \tag{6}$$

where d is membrane thickness, and p_2 and p_1 are feed-side and permeate-side $p(O_2)$, respectively. Since this term is proportional to $j \times d$ by definition, its value is thickness-independent when surface-exchange limitations are negligible but increases with thickness when they become significant [8,9,22]. The latter situation is observed for undoped $La_{0.5}Sr_{0.5}FeO_{3-\delta}$, where the role of exchange kinetics increases with decreasing temperature (Fig. 11), and for $(La_{0.5}Sr_{0.5})_{0.97}FeO_{3-\delta}$.

In the case of $La_{0.5}Sr_{0.5}Fe_{0.9}Al_{0.1}O_{3-\delta}$, the specific permeability is almost thickness-independent at 1123–1223 K (Fig. 11d), indicating that oxygen transport at this temperature is limited mainly by bulk ionic conductivity. At lower temperatures, the permeation-limiting effect of surface exchange tends to increase, but still remains comparable to the measurement error. The behavior of all other Al-containing materials studied in this work was found similar to $La_{0.5}Sr_{0.5}Fe_{0.9}Al_{0.1}O_{3-\delta}$, with negligible surface limitations when the membrane thickness is larger than 0.6 mm. This makes it possible to calculate the oxygen ionic conductivity of Al-containing phases from the permeation data. The values of σ_O, calculated from the OP results as described in previous works [8,9,14], show a good agreement with the FE measurements (Fig. 13), thus confirming validity of such estimations. In the case of
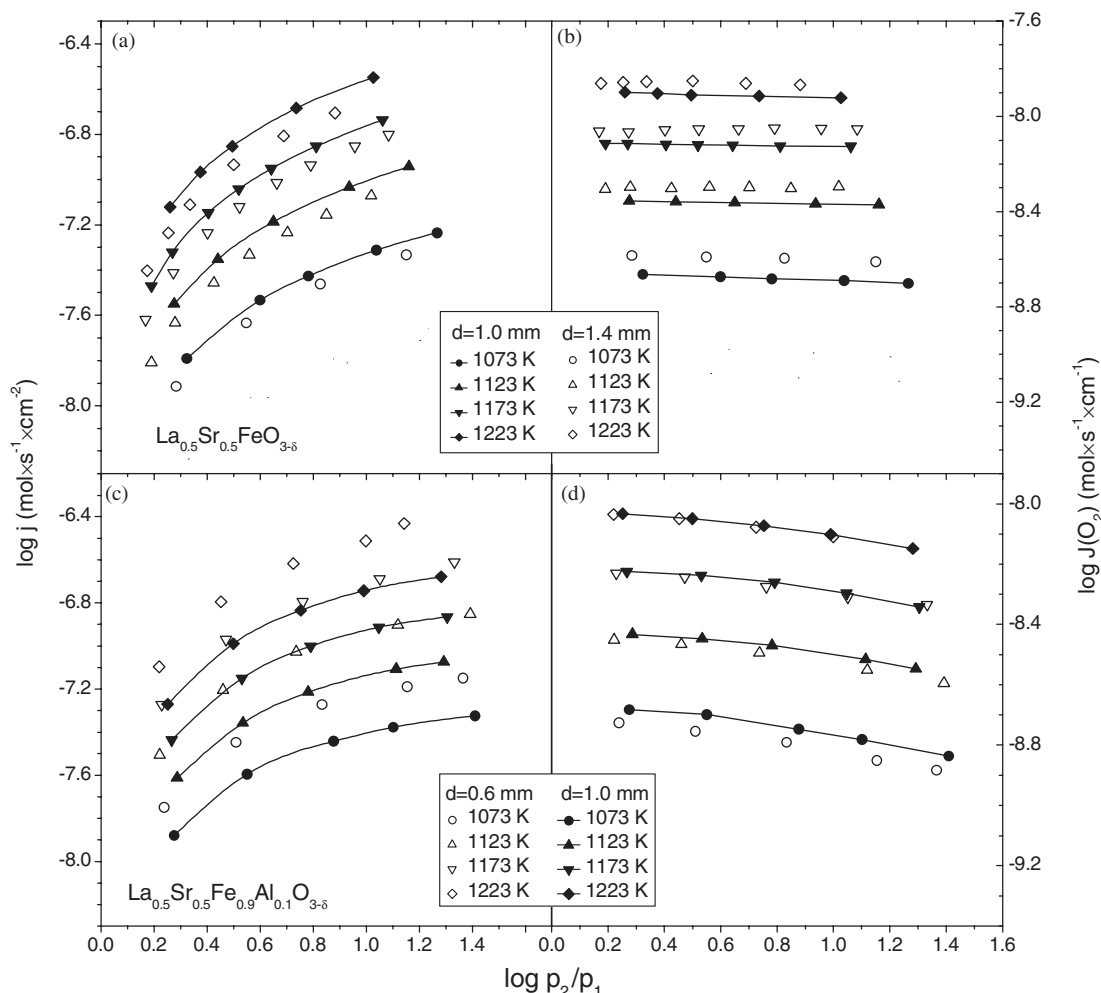
Fig. 11. Oxygen permeation fluxes (a,c) and specific oxygen permeability (b,d) of dense ceramic $La_{0.5}Sr_{0.5}FeO_{3-\delta}$ (a,b) and $La_{0.5}Sr_{0.5}Fe_{0.9}Al_{0.1}O_{3-\delta}$ (c,d) membranes.
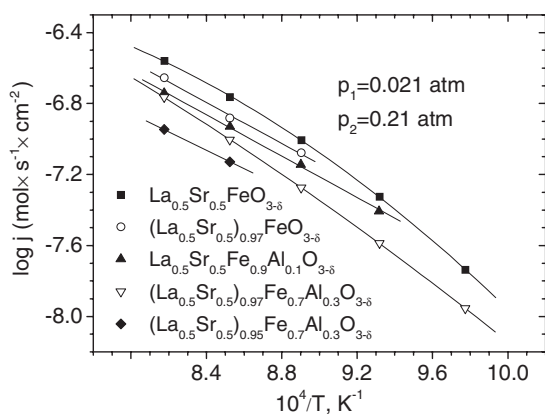

Fig. 12. Temperature dependence of the oxygen permeation fluxes through $(La_{0.5}Sr_{0.5})_{1-x}Fe_{1-y}Al_yO_{3-\delta}$ membranes under fixed oxygen pressure gradient. Membrane thickness is 1.00 ± 0.02 mm.
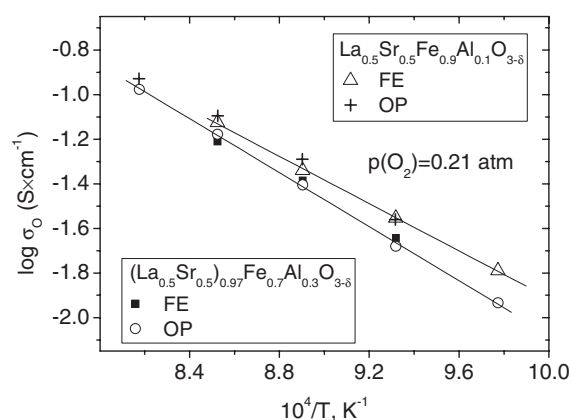

Fig. 13. Comparison of the ionic conductivity values calculated from the oxygen permeation (OP) and faradaic efficiency (FE) results. All data correspond to the membrane thickness of 1.0 mm.

$La_{0.5}Sr_{0.5}FeO_{3-\delta}$ where the effect of exchange kinetics is significant, the σ_O estimates are lower than true values and can only be used to assess qualitatively the general relationships between composition and ionic transport.

One may also mention that the data shown in Figs. 11 and 12 reflect a general correlation between the level of oxygen permeability and the relative role of surface exchange kinetics observed for most ferrite membranes [9]. Namely,
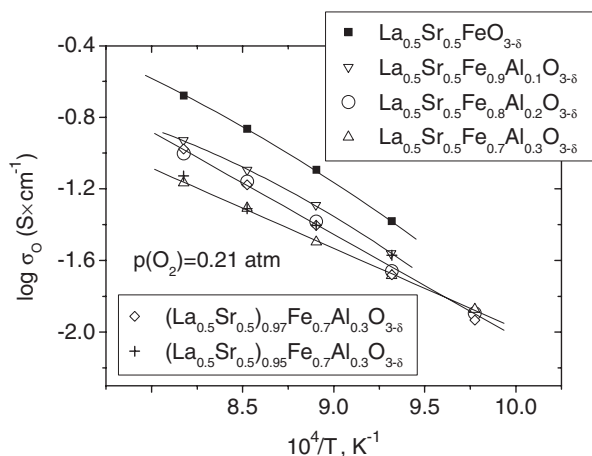
Fig. 14. Oxygen ionic conductivity of $(La_{0.5}Sr_{0.5})_{1-x}Fe_yAl_{1-y}O_{3-\delta}$ ceramics in air.

Fig. 15. Oxygen ion transference numbers of $La_{0.5}Sr_{0.5}FeO_3$-based materials in air.

an increase in ionic conductivity of ferrite-based materials leads, as expected, to increasing oxygen permeability, but the effect of surface exchange rates on the permeation also increases.

Temperature dependencies of the oxygen ionic conductivity of $(La_{0.5}Sr_{0.5})_{1-x}Fe_{1-y}Al_yO_{3-\delta}$ in air are presented in Fig. 14; Table 3 lists the respective activation energies. Note, once again, that the σ_O values of undoped $La_{0.5}Sr_{0.5}FeO_{3-\delta}$ should be considered as estimations only. Nevertheless, these data clearly show that ionic transport in the A-site stoichiometric compositions decreases with increasing aluminum content. Such a behavior is similar to that in $(La,Sr)FeO_{3-\delta}$ system [11], where a high Sr concentration induces ordering in the oxygen sublattice. An analogous mechanism seems responsible for the relatively low ionic conduction in Al-substituted $La_{0.5}Sr_{0.5}FeO_{3-\delta}$, particularly due to small size of Al^{3+} cations [27] which may promote vacancy clustering. As for $Sr(Fe,Ti)O_{3-\delta}$ perovskites [22], the creation of 3% cation vacancies in the A sublattice of $La_{0.5}Sr_{0.5}Fe_{0.7}Al_{0.3}O_{3-\delta}$ leads to a faster ionic transport at 1123–1223 K; higher A-site deficiency has a negative effect. The deviations from Arrhenius dependence, observed for ionic conductivity of $(La_{0.5}Sr_{0.5})_{0.95}Fe_{0.7}Al_{0.3}O_{3-\delta}$, are probably caused by changes in the phase composition with temperature. The oxygen ion transference numbers of $(La_{0.5}Sr_{0.5})_{1-x}Fe_{1-y}Al_yO_{3-\delta}$ ceramics at 973–1223 K and atmospheric oxygen pressure vary in the range 1×10^{-4}–3×10^{-3}, increasing with temperature (Fig. 15).

The hypothesis on the transport-limiting role of vacancy ordering processes is supported by the data on oxygen-ionic conductivity in reducing atmospheres, calculated by fitting the $p(O_2)$-dependencies of the total conductivity; one example is presented in Fig. 16. For undoped $La_{0.5}Sr_{0.5}FeO_{3-\delta}$ with essentially disordered oxygen sublattice, decreasing oxygen pressure from atmospheric down to 10^{-14}–10^{-8} atm leads to 2–6 times higher ionic conduction. On the contrary, the ionic transport in
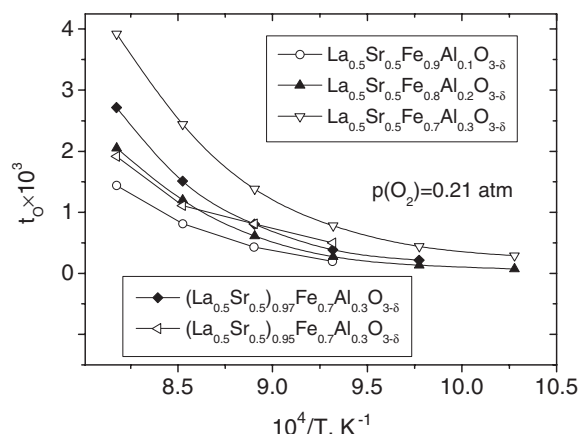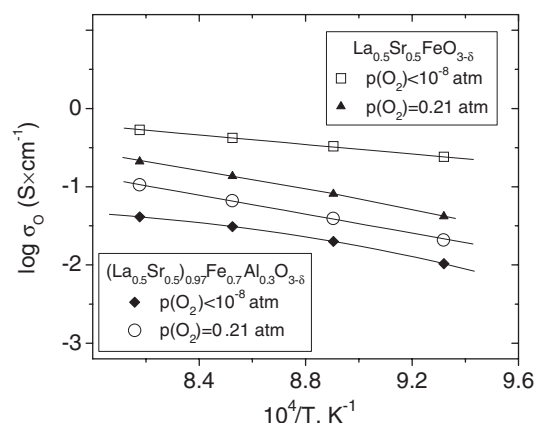

Fig. 16. Comparison of the oxygen ionic conductivity of $La_{0.5}Sr_{0.5}FeO_{3-\delta}$ and $(La_{0.5}Sr_{0.5})_{0.97}Fe_{0.3}Al_{0.3}O_{3-\delta}$ in air and under reducing conditions.

$(La_{0.5}Sr_{0.5})_{0.97}Fe_{0.7}Al_{0.3}O_{3-\delta}$ decreases on reduction, whilst the activation energy is almost unchanged. These trends indicate that most vacancies in the Al-substituted ferrite are trapped in defect clusters or locally ordered microdomains stable even at elevated temperatures, such as 1223 K. As for Sr and Al doping, increasing total oxygen nonstoichiometry on reducing $p(O_2)$ induces further ordering in the oxygen sublattice, where the concentration of mobile vacancies is exclusively determined by temperature-activated disordering processes. Regardless of the ionic charge-carrier formation mechanisms, the results show that the influence of A-site deficiency on the ionic conductivity cannot be attributed to the oxygen nonstoichiometry variations and results, most likely, from increasing structural disorder. One possible reason may relate to local distortions near the cation vacancies. Although these lattice defects should reduce the mobility of neighboring oxygen ions and vacancies, their random distribution in the perovskite-type structure may suppress partial ordering.

5. Conclusions

In order to identify the effects of alumina additions and minor A-site cation deficiency on the properties of lanthanum–strontium ferrites with high oxygen-ionic conductivity, selected compositions in the system $(La_{0.5}Sr_{0.5})_{1-x}Fe_{1-y}Al_yO_{3-\delta}$ ($x = 0-0.05$, $y = 0-0.30$) have been appraised employing XRD, SEM/EDS, Mössbauer spectroscopy, dilatometry, CT, and measurements of the total conductivity and Seebeck coefficient in the oxygen partial pressure range 10^{-20} to 0.5 atm. Aluminum incorporation was found to decrease the unit cell volume and partial ionic and p-type electronic conductivities, while the oxygen nonstoichiometry and thermal expansion at 900–1200 K increase on doping. The transport properties of Al-substituted ferrite may be improved by the creation of A-site cation vacancies, probably promoting disordering in the oxygen sublattice. However, the maximum A-site deficiency in $La_{0.5}Sr_{0.5}Fe_{1-y}Al_yO_{3-\delta}$ is limited, close to 3–4% at $y = 0.3$. The Mössbauer spectroscopy data show progressive localization of electron holes and a mixed charge-compensation mechanism, which results in higher average oxidation state of iron when Al^{3+} concentration increases. The average thermal expansion coefficients of $(La_{0.5}Sr_{0.5})_{1-x}Fe_{1-y}Al_yO_{3-\delta}$ are $(12.2-13.0) \times 10^{-6}\,K^{-1}$ at 300–900 K and $(20.1-30.0) \times 10^{-6}\,K^{-1}$ at 900–1200 K in air. The oxygen permeability of ceramic materials with $y \geqslant 0.1$ is determined mainly by the bulk ionic conductivity. The oxygen ion transference numbers, calculated from the OP and FE data at 973–1223 K, vary in the range 1×10^{-4}–3×10^{-3}, increasing with temperature.

References

[1] H.J.M. Bouwmeester, A.J. Burgraaf, in: A.J. Burgraaf, L. Cot (Eds.), Fundamentals of Inroganic Membrane Science and Technology, Elsevier, Amsterdam, 1996, p. 435.
[2] P.N. Dyer, R.E. Richards, S.L. Russek, D.M. Taylor, Solid State Ionics 134 (2000) 21.
[3] T.J. Mazanec, R. Prasad, R. Odegard, C. Steyn, E.T. Robinson, Stud. Surf. Sci. Catal. 136 (2001) 147.
[4] D.J. Wilhelm, D.R. Simbeck, A.D. Karp, R.L. Dickenson, Fuel Process. Technol. 71 (2001) 139.
[5] A. Thursfield, I.S. Metcalfe, J. Mater. Chem. 14 (2004) 2475.
[6] J.E. ten Elshof, H.J.M. Bouwmeester, H. Verweij, Solid State Ionics 81 (1995) 97.
[7] J.E. ten Elshof, H. Verweij, Solid State Ionics 89 (1996) 81.
[8] V.V. Kharton, A.L. Shaulo, A.P. Viskup, M. Avdeev, A.A. Yaremchenko, M.V. Patrakeev, A.I. Kurbakov, E.N. Naumovich, F.M.B. Marques, Solid State Ionics 150 (2002) 229.
[9] V.V. Kharton, A.A. Yaremchenko, A.L. Shaula, A.P. Viskup, F.M.B. Marques, J.R. Frade, E.N. Naumovich, J.R. Casanova, I.P. Marozau, Defect Diffus. Forum 226–228 (2004) 141.
[10] E.V. Tsipis, M.V. Patrakeev, V.V. Kharton, A.A. Yaremchenko, G.C. Mather, A.L. Shaula, I.A. Leonidov, V.L. Kozhevnikov, J.R. Frade, Solid State Sci. 7 (2005) 355.
[11] M.V. Patrakeev, J.A. Bahteeva, E.B. Mitberg, I.A. Leonidov, V.L. Kozhevnikov, K.R. Poeppelmeier, J. Solid State Chem. 172 (2003) 219.
[12] T.J. Mazanec, in: H.U. Anderson, A.C. Khandkar, M. Liu (Eds.), Ceramic Membranes IPV95-24, The Electrochemical Society, Pennington, NJ, 1997, p. 16.
[13] M. Schwartz, J.H. White, A.F. Sammells, US patent 6214757, 2001.
[14] V.V. Kharton, A.V. Kovalevsky, A.P. Viskup, J.R. Jurado, F.M. Figueiredo, E.N. Naumovich, J.R. Frade, J. Solid State Chem. 156 (2001) 437.
[15] J.T. Ritchie, J.T. Richardson, D. Luss, AIChE J 47 (2001) 2092.
[16] V.V. Kharton, A.A. Yaremchenko, M.V. Patrakeev, E.N. Naumovich, F.M.B. Marques, J. Eur. Ceram. Soc. 23 (2003) 1417.
[17] M.V. Patrakeev, E.B. Mitberg, A.A. Lakhtin, I.A. Leonidov, V.L. Kozhevnikov, V.V. Kharton, M. Avdeev, F.M.B. Marques, J. Solid State Chem. 167 (2002) 203.
[18] A.A. Yaremchenko, M.V. Patrakeev, V.V. Kharton, F.M.B. Marques, I.A. Leonidov, V.L. Kozhevnikov, Solid State Sci. 6 (2004) 357.
[19] Q. Ming, J. Huang, Y.L. Yang, M. Nersesyan, A.J. Jacobson, J.T. Richardson, D. Luss, Combust. Sci. Technol. 138 (1998) 279.
[20] V.V. Kharton, A.L. Shaula, F.M.M. Snijkers, J.F.C. Cooymans, J.J. Luyten, A.A. Yaremchenko, A.A. Valente, E.V. Tsipis, J.R. Frade, F.M.B. Marques, J. Rocha, J. Membrane Sci. 252 (2005) 215.
[21] K. Yamaji, T. Horita, M. Ishikawa, N. Sakai, H. Yokokawa, Solid State Ionics 121 (1999) 217.
[22] V.V. Kharton, A.V. Kovalevsky, E.V. Tsipis, A.P. Viskup, E.N. Naumovich, J.R. Jurado, J.R. Frade, J. Solid State Electrochem. 7 (2002) 30.
[23] J. Rodrígues-Carvajal, Physica B 192 (1993) 55.
[24] A.C. Larson, R.B. Von Dreele, General Structure Analysis System (GSAS), Los Alamos National Laboratory Report LAUR 86-748 (2004).
[25] J.C. Waerenborgh, M.O. Figueiredo, J.M.P. Cabral, L.C.J. Pereira, Phys. Chem. Miner. 21 (1994) 460.
[26] J. Hesse, A. Rübartsch, J. Phys. E 7 (1974) 526.
[27] R.D. Shannon, Acta Crystallogr. A 32 (1976) 751.
[28] J. Holc, D. Kuščer, M. Hrovat, S. Bernik, D. Kolar, Solid State Ionics 95 (1997) 259.
[29] G.W. Coffey, J. Hardy, L. Pedersen, P.C. Rieke, E.C. Thomsen, M. Walpole, Solid State Ionics 158 (2003) 1.
[30] S.E. Dann, D.B. Currie, M.T. Weller, M.F. Thomas, A.D. Al-Rawwas, J. Solid State Chem. 109 (1994) 134.
[31] P. Adler, S. Eriksson, Z. Anorg, Allg. Chem. 626 (2000) 118.
[32] J.C. Waerenborgh, D.P. Rojas, A.L. Shaula, G.C. Mather, M.V. Patrakeev, V.V. Kharton, J.R. Frade, Mater. Lett. 59 (2005) 1644.
[33] P. Adler, S. Gnosh, Solid State Sci. 5 (2003) 445.
[34] V.V. Kharton, J.C. Waerenborgh, D.P. Rojas, A.A. Yaremchenko, A.A. Valente, A.L. Shaula, M.V. Patrakeev, F.M.B. Marques, J. Rocha, Catal. Lett. 99 (2005) 249.
[35] P. Adler, J. Mater. Chem. 9 (1999) 471.
[36] J. Mizusaki, M. Yoshihiro, S. Yamauchi, K. Fueki, J. Solid State Chem. 58 (1985) 257.
[37] H.U. Anderson, Solid State Ionics 52 (1992) 33.
[38] H.-H. Möbius, in: Ext. Abstr. 37th Meeting of Int. Society of Electrochemistry, Vilnius, Lithuania, 1986, Vol. 1, p. 136.